Journal of Oceanology and Limnology
Vol. 36 No. 6, P. 2110-2129, 2018
https://doi.org/10.1007/s00343-019-7301-3

Interannual wave climate variability in the Taiwan Strait and its relationship to ENSO events*

OU Yanda (欧衍达), ZHAI Fangguo (翟方国)**, LI Peiliang (李培良)

Ocean University of China, *Qingdao 266100*, *China*

Received Oct. 29, 2017; accepted in principle Dec. 7, 2017; accepted for publication Dec. 15, 2017

Abstract This study investigated the interannual wave climate variability in the Taiwan Strait (TS) and its relationship to the El Niño-Southern Oscillation (ENSO) phenomenon using a high-resolution numerical wave model. The results showed the interannual variability of significant wave height (SWH) in the TS, which exhibits significant spatial and seasonal variations, is typically weaker than the seasonal variability. The standard deviation of the interannual SWH anomaly (SWHA) showed similar spatial variations in the TS throughout the year, being largest in the middle of the strait and decreasing shoreward, except in summer, when there was no local maximum in the middle of the TS. Further analyses proved the interannual wave climate variability in the TS is controlled predominantly by tropical cyclone activities in summer and by the northeasterly monsoon winds in winter. Furthermore, the interannual SWHA in the TS was found correlated highly negatively with the ENSO phenomenon. This relationship mainly derives from that during the northeasterly monsoon seasons. During the northeasterly monsoon seasons in El Niño (La Niña) years, the negative (positive) SWHA in the TS derives from weakened (strengthened) northeasterly monsoon winds induced by a lower-tropospheric anomalous anticyclone (cyclone) over the western Pacific Ocean and the South China Sea. During the southwesterly monsoon season in El Niño (La Niña) years, however, the SWH in the TS tends to increase (decrease) anomalously because of intensified (weakened) TC activities over the western North Pacific Ocean and adjacent seas.

Keyword: significant wave height (SWH); Taiwan Strait; interannual variability; El Niño-Southern Oscillation (ENSO)

1 INTRODUCTION

The Taiwan Strait (TS), located between mainland China and Taiwan Island, is a narrow channel that connects the East China Sea (ECS) and the South China Sea (SCS) (Jan et al., 2002, 2010; Feng et al., 2010). It is dominated by the East Asia monsoon system, with the sea surface wind flowing from the northeast in winter and from the southwest in summer (Jan et al., 2002; Guo et al., 2010). Because of the so-called 'narrow pipe effect', the TS is an environment of very complex ocean dynamics (Zheng et al., 2016). Among others, surface gravity waves are deemed to have considerable impact both on shipping security and on the coastal ecosystem and its management (Yamaguchi et al., 2002; Bromirski et al., 2013; Zheng et al., 2015; Zhou et al., 2015). However, few previous studies have considered the spatiotemporal variations and associated dynamics of surface gravity waves in this region.

Based on satellite observations, Chen et al. (2006) reported that the TS is one of the regions with the largest waves in China's offshore waters and the adjacent seas. They also demonstrated that the significant wave height (SWH) in the TS has considerable seasonal variation, being largest in winter and smallest in summer. Forced by the East Asia monsoon system, surface gravity waves in the TS are dominated by strong northeasterly waves in winter, whereas they are affected by relatively weaker

* Supported by the National Natural Science Foundation of China (Nos. 41506008, 41476002), the Shandong Provincial Natural Science Foundation (No. ZR2015DQ006), and the Shandong Provincial Key Research and Development Program (No. 2016ZDJS09A02)
**Corresponding author: gfzhai@ouc.edu.cn

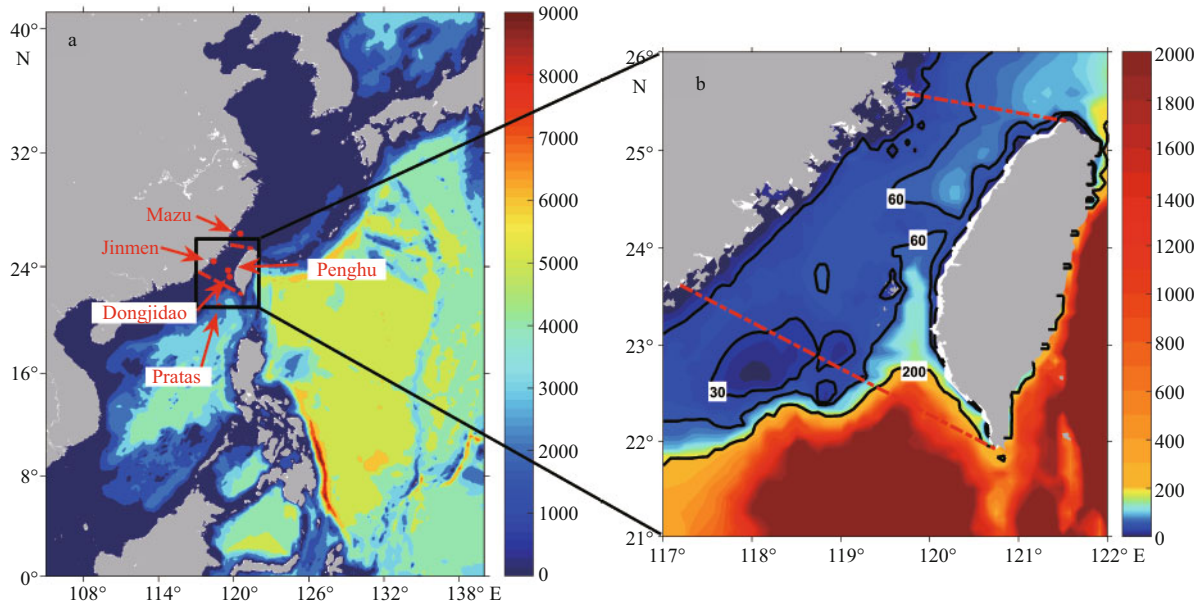

Fig.1 Bathymetry (unit: m) of (a) the entire computation domain and (b) the TS

Red dashed lines represent the northern and southern boundaries of the TS. In (a), the red dots denote buoy stations. In (b), only ocean regions shallower than 2 000 m are shown.

southwesterly-southerly waves in summer (Chen et al., 2006; Guo et al., 2010). Moreover, the wave directions are more complex in summer than in winter (Zhang et al., 2002). The SWH in the TS has also been proven to have considerable interannual variation based on both satellite observations (Chen et al., 2006) and numerical simulations (Hwang et al., 2010; Chien et al., 2014). Using the same satellite observations, Chen et al. (2006) stated that they found a pronounced period of variability of about five years in SWH in the TS, which might correspond to the El Niño-Southern Oscillation (ENSO; Wang et al., 2016). Considerable interannual variability of SWH in the TS has also been noted by Hwang et al. (2010) and by Chien et al. (2014) following high-resolution numerical simulations.

Many questions remain to be resolved concerning the interannual wave climate variability in the TS. First, even though Chien et al. (2014) reported the interannual variability of SWH at Longdong station, located to the northwest of Taiwan Island, the spatiotemporal variations of SWH over the entire TS remain largely unknown. Second, the underlying dynamics also remain unknown. In winter, surface gravity waves in the TS are forced by northeasterly monsoon winds (Lin and Fang, 2012); however, in summer, they are forced both by southwesterly monsoon winds and by frequent tropical cyclone (TC) activities (Chang and Chien, 2001; Chan, 2005). Therefore, the dynamics responsible for the interannual wave climate variability in the TS might differ between these two seasons. Finally, although a potential relationship of interannual wave climate variability in the TS with the ENSO phenomenon has been proposed by previous studies (Chen et al., 2006; Hwang et al., 2010), the precise characteristics of the driving mechanisms remain unclear.

The objective of the current study was to investigate the interannual wave climate variability in the TS based on high-resolution simulations using a regional ocean wave model. This remainder of the paper is arranged as follows. In Section 2, the model setup, relevant data, and methods adopted in the current study are described in detail. In Section 3, the model outputs are validated against observations. The results obtained and the conclusions derived are presented in Section 4 and 5, respectively.

2 MODEL, OBSERVATION, AND METHOD

2.1 Wave model

The present study used the third-generation Simulating WAves Nearshore (SWAN; Booij et al., 1999) model version 40.91 to hindcast the historical wave records in the western Pacific Ocean for the period from January 1979 to July 2016. As shown in Fig.1a, the computational domain (0°–41°N, 105°–140°E) covered the China seas (namely, the Bohai Sea, Yellow Sea, ECS, and SCS) and part of the western North Pacific Ocean. The spatial and temporal

Table 1 Buoy observations in the TS

Buoy station	Location	Water depth (m)	Sea surface wind speed	SWH
Dongjidao	119.68°E, 23.26°N	20.0	-	20140706–20160731
Jinmen	118.41°E, 24.38°N	25.0	20140706–20160731	20140706–20160731
Mazu	120.54°E,26.38°N	58.0	20140827–20160731	20140827–20160731
Penghu	119.55°E,23.73°N	26.6	20140706–20160731	20140706–20160731
Pratas	118.82°E,21.07°N	2618.0	20140706–20151222	20140706–20151222

"-" means no data.

computational resolutions were 0.2°×0.2° and 1 h, respectively. The resolution of the spectral domain was defined as 0.04–1.0 Hz, divided into 34 bands. The directional resolution was set to 10°. Default schemes and parameter values were adopted for the key physical processes in the wave model. An exponential growth of wind input was adopted using the expression of Komen et al. (1984). Dissipation processes in the wave model included whitecapping, depth-induced breaking, and bottom friction. The formulation of Komen et al. (1984) was applied for the whitecapping process with a dissipation coefficient of 2.36×10^{-5}. The formulation of Battjes and Janssen (1978) was applied for depth-induced wave breaking. The proportionality coefficient of the rate of dissipation and the ratio of maximum individual wave height over depth were set to 1.0 and 0.73, respectively. The empirical model of JONSWAP from Hasselmann et al. (1973) was applied for bottom dissipation adopting friction coefficient values of 0.038 and 0.067 m^2/s^3 for swell conditions and wind sea conditions, respectively. A lumped triad approximation scheme (Eldeberky, 1996) and a discrete interaction approximation scheme (Hasselmann et al., 1985) were used for the triad and quadruplet wave-wave interaction processes, respectively.

The bathymetric data used in the wave model were obtained from the ETOPO5 bathymetry database of the National Oceanic and Atmospheric Administration/ National Geophysical Data Center, which can be downloaded via https://www.ngdc.noaa.gov/mgg/global/etopo5.HTML. The horizontal resolution of the ETOPO5 database is 5′×5′. The wave model was forced with wind vectors at 10 m above the sea surface derived from the European Centre for Medium-Range Weather Forecasts Interim reanalysis (ERA-I; Dee et al., 2011). The sea surface wind vectors are provided at UTC 00, 06, 12, and 18 with spatial resolution of 0.125°×0.125°.

In addition to the high-resolution SWH, mean wave direction, and mean wave period derived from the ERA-I global reanalysis, parametric spectra in the shape of a JONSWAP spectrum (Hasselmann et al., 1973) were defined at all ocean boundaries. Therefore, under the model configuration adopted, sea surface gravity waves in the TS were not only forced by the local sea surface wind in the TS but also by the winds in the ECS, SCS, and Pacific Ocean. The wave parameters of interest were output every 6 h on a 0.2°×0.2° grid.

2.2 Observation

Before conducting in-depth analyses, it was considered prudent to evaluate the results derived from the wave model against observations. For that purpose, we adopted wave height observations from both buoys and satellites. The red dots in Fig.1a show the locations of the buoy stations considered, and detailed descriptions of the buoy observations are given in Table 1. The buoy observations were provided by the Central Weather Bureau of Taiwan and they can be downloaded via http://www.cwb.gov.tw/V7. Of the buoy stations considered for verification, sea surface wind speed was observed at Jinmen, Mazu, Penghu, and Pratas. The buoy observations used here covered a limited period from July 2014 to July 2016 with a 1-h sampling interval.

Satellite observations were also used. These included near real-time merged SWH (NRT-SWH) and delayed-time along track SWH observed by Topex/Poseidon, Jason-1, and Jason-2. The NRT-SWH data were provided on a global 1.0°×1.0° grid with a time interval of one day. The satellite missions used to prepare the NRT-SWH included ERS-1 and 2, Jason-1, 2, and 3, Envisat, Cryosat, HY-2, and Saral to ensure at least two missions were available for the generation of a merged map. Blended SWH observations were then cross-calibrated using OSTM/ Jason-2 as the reference mission. In the current study, the NRT-SWH data extended from October 2009 to July 2016, while the along track SWHs observed by Topex/Poseidon, Jason-1, and Jason-2 extended from

Table 2 Comparison between the simulated (SWAN model) SWHs and observed (buoy) SWHs

Buoy name	*R*	Mean (m)		Bias (m)	SI
		SWAN	Observation		
Dongjidao	0.86	1.06	1.18	-0.12	0.69
Jinmen	0.87	0.82	0.91	-0.09	0.55
Mazu	0.88	1.38	1.49	-0.11	0.59
Penghu	0.88	1.09	0.96	0.13	0.62
Pratas	0.89	1.79	1.89	-0.10	0.55

All linear correlation coefficients presented are above the 95% confidence level.

September 1992 to October 2005, from January 2002 to June 2013, and from June 2008 to July 2016, respectively. All satellite observations were provided by AVISO.

To examine the impact of the TC activities on the interannual wave climate variability in the TS, the TC best-track dataset was used. This is prepared by the Regional Specialized Meteorological Center of the Tokyo Typhoon Center and it includes the 6-hourly positions (TC latitude and longitude), intensity grades, and central pressures of those TCs appearing in the western North Pacific Ocean during January 1979 to July 2016.

To investigate the possible relationship between the wave climate variability in the TS and the ENSO phenomenon, the sea surface temperature anomaly averaged over the Niño-3.4 region was used as the ENSO index. For the current study, the ENSO index, downloaded via https://www1.ncdc.noaa.gov/pub/data/cmb/ersst/v4/index was calculated using the Extended Reconstructed Sea Surface Temperature dataset version 4 (Huang et al., 2014).

2.3 Method

It has been proven that the wave energy per unit surface area (E; unit: J/m^2) is proportional to the square of the combined SWH (Chen et al., 2002; Jiang and Chen, 2013):

$$E=\rho g(H^2_M/32),$$

where ρ, g, E, and H_M denote the reference sea water density, gravitational acceleration, wave energy, and combined SWH, respectively. Here, ρ was set to 1 025 kg/m^3 and g was set as 9.81 m/s^2. Thus, the wave energy in the TS during different periods of each month could be estimated accordingly. For example, in August 1992, TCs influenced the TS (See Section 4.3.1 for more details) on about 14 d. Therefore, the wave energy with TC influence during this month was estimated as the sum of E during those 14 d, while the wave energy without TC influence was obtained by summing the wave energy during the rest of the month.

In the current study, the interannual anomalies of the variables of interest were calculated as follows. For monthly variables, monthly mean anomalies were obtained through subtracting the monthly climatology from the original monthly means. Then, a 13-month running mean filter was applied to exclude subannual signals.

3 MODEL VALIDATION

3.1 Comparison with buoy observations

A comparison of the 6-hourly SWHs hindcasted by the high-resolution SWAN model and those observed by buoys is shown in Fig.2. Overall, the model hindcasted SWHs agree reasonably well with the buoy observations in terms of both magnitude and temporal phase. Their simultaneous correlations are all >0.85 above the 95% confidence level at the five buoy stations. The mean biases (Table 2), computed as the model results subtracting the buoy observations, indicate that the wave model slightly underestimates SWH at most buoy stations, especially when the waves are large. At Penghu station, however, the wave model slightly overestimates SWH during most of the observation period. Nonetheless, the biases are considerably low when compared with the mean SWH. The ratios of the biases to the observed SWHs are <10% in their magnitudes at most buoy stations, and the scatter indexes (SIs) are also low, i.e., in the range 0.55–0.69.

A comparison of the 6-hourly sea surface wind speeds derived from the ERA-I global reanalysis and those observed at four of the buoy stations is presented in Fig.3. Overall, these two data sets of sea surface wind speed agree reasonably well in terms of both temporal phase and magnitude. The simultaneous correlations between them at the four buoy stations range from 0.79 to 0.86 above the 95% confidence level. Moreover, the mean wind speeds from the ERA-I global reanalysis and buoy observations are both about 5.82–6.92 m/s (Table 3). However, we also note that the ERA-I global reanalysis slightly underestimates the observed sea surface wind speeds at the Jinmen and Mazu buoy stations with biases of about -0.27 and -0.66 m/s, respectively. Conversely, the observations at the Penghu and Pratas buoy stations are slightly overestimated with biases of up to 0.51 and 0.07 m/s, respectively. However, the biases

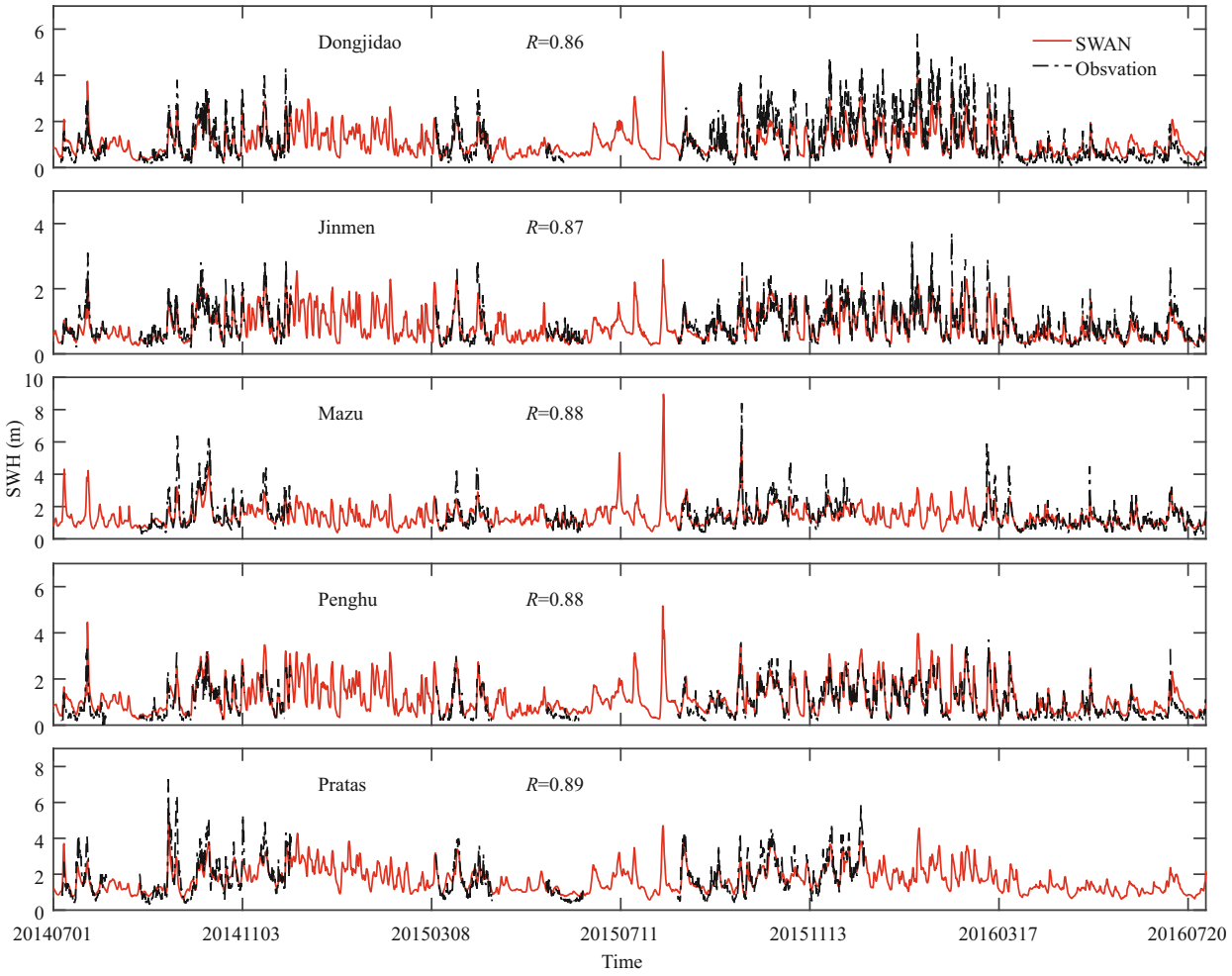

Fig.2 Six-hourly SWH (unit: m) output by the wave model (red line) and that observed by buoys (black dashed line) at the Dongjidao, Jinmen, Mazu, Penghu, and Pratas buoy stations

In each panel, the number denotes the simultaneous linear correlation between the two time series.

are rather low compared with the mean values. The ratios of the biases to mean values are 1.02%–9.54% in terms of magnitude, and the SIs at the four buoy stations are also generally low, i.e., about 0.48–0.57.

3.2 Comparison with satellite observations

A comparison of the model simulation and satellite observations is presented in Fig.4, from which it can be seen that the wave model hindcast agrees reasonably well with the satellite observations. Their SIs are generally low, ranging from 0.26 to 0.29; however, it should be noted that the least squares fitted slopes between the model hindcast and satellite observations are 0.80 for NRT-SWH and 0.77 for all delayed-time SWHs. This means the hindcasted SWHs are slight underestimates in comparison with the satellite observations.

The simultaneous linear correlation coefficient between the daily time series of the hindcast SWH and NRT-SWH is shown in Fig.4e. In the far western North Pacific Ocean and the adjacent China seas, the correlations are much larger than 0.70 above the 95% confidence level, indicating reasonably good agreement between their temporal fluctuations. In the adjacent China seas, the correlation is much larger than 0.86 in most areas of the SCS, and between 0.70 and 0.80 in most regions of the ECS and the Yellow Sea.

Table 3 Same as Table 2 but for the wind speed at 10 m above the sea surface

Buoy Names	CC	Mean (m/s)		Bias (m/s)	SI
		ERA-I	Obs.		
Jinmen	0.79	5.82	6.09	-0.27	0.57
Mazu	0.81	6.25	6.92	-0.66	0.53
Penghu	0.87	6.67	7.18	0.51	0.55
Pratas	0.86	6.90	6.83	0.07	0.48

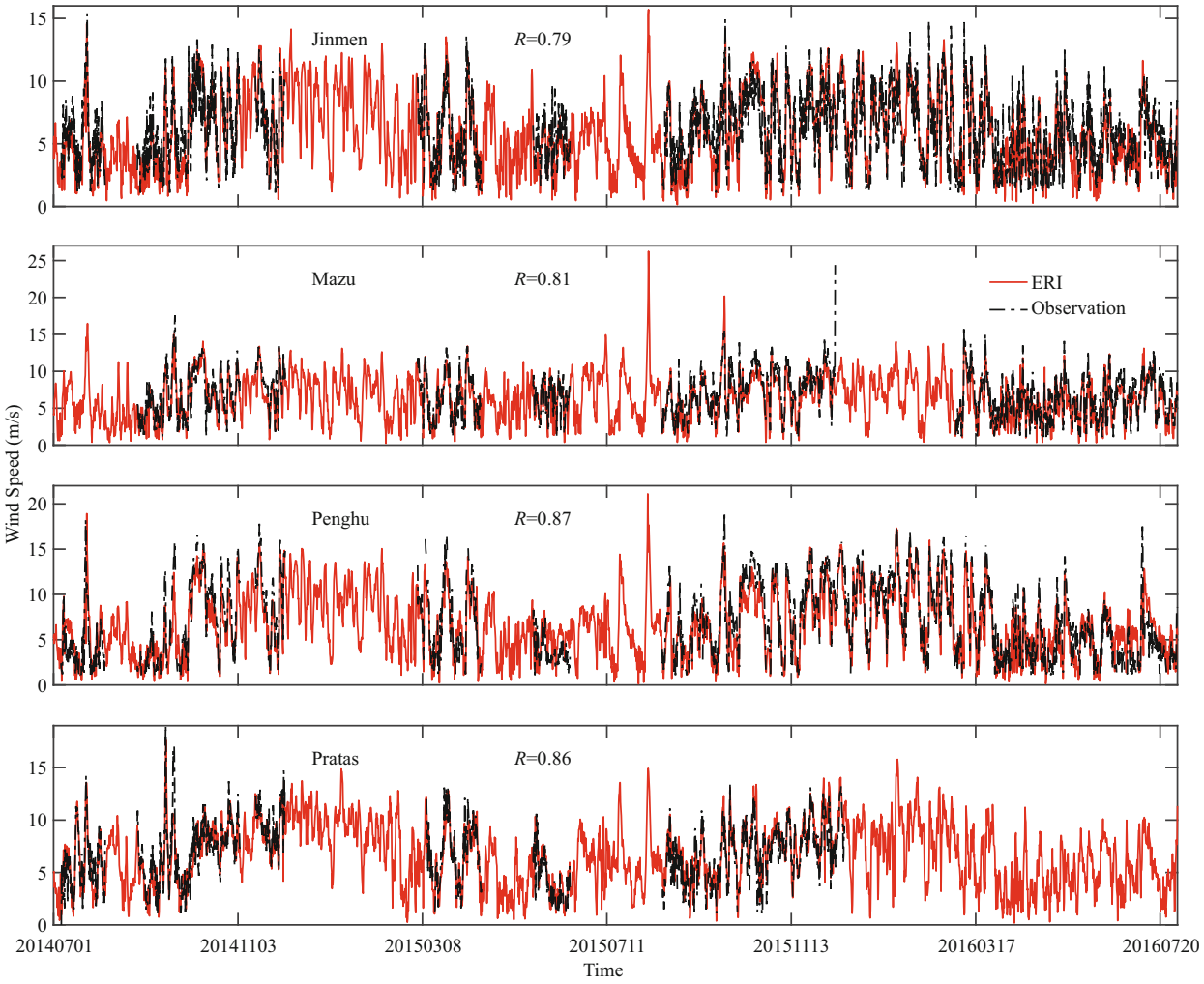

Fig.3 Same as Fig.2 but for the 6-hourly wind speed (unit: m/s) at 10 m above the sea surface

Based on the above analyses, it was concluded that the SWAN model was capable of reproducing the SWH variations in the regions of interest. However, it should be noted that the wave model results generally underestimate the observed SWH. One possible reason is that we adopted the default parameter values in the model, which might tend to produce SWHs smaller than the observations (Jiang et al., 2014).

4 RESULT

4.1 Seasonal variability

The climatological mean SWH over the entire study period is shown in Fig.5a. It can be seen that SWH is largest in the western North Pacific Ocean and it then decreases toward the adjacent China seas. There are two tongues of high SWH: one extending northward into the ECS and the other extending westward into the SCS. The SWH in the TS, however, is relatively small. As shown in Fig.5b, the largest SWH in the TS, which is about 1.40 m, occurs around the middle of the strait with SWHs then decreasing shoreward. The area-averaged SWH in the TS is only about 1.19 m, much lower than in the western North Pacific Ocean at the same latitude. Across the northern and southern boundaries of the TS, there are two tongues of high SWH: one extending southward from the ECS and the other extending northward from the SCS, respectively. This might imply that the wave climate in the TS is possibly influenced by that in the ECS, SCS, and even the western North Pacific Ocean. The standard deviation (SD) of the monthly SWH (Fig.5c) shows a rather different spatial distribution from that of the climatological mean SWH. In the western North Pacific Ocean and adjacent China seas, the SD of the SWH has two regions of high values well above 0.5 m, which are located east of Luzon and along a northeast-southwest band extending from the

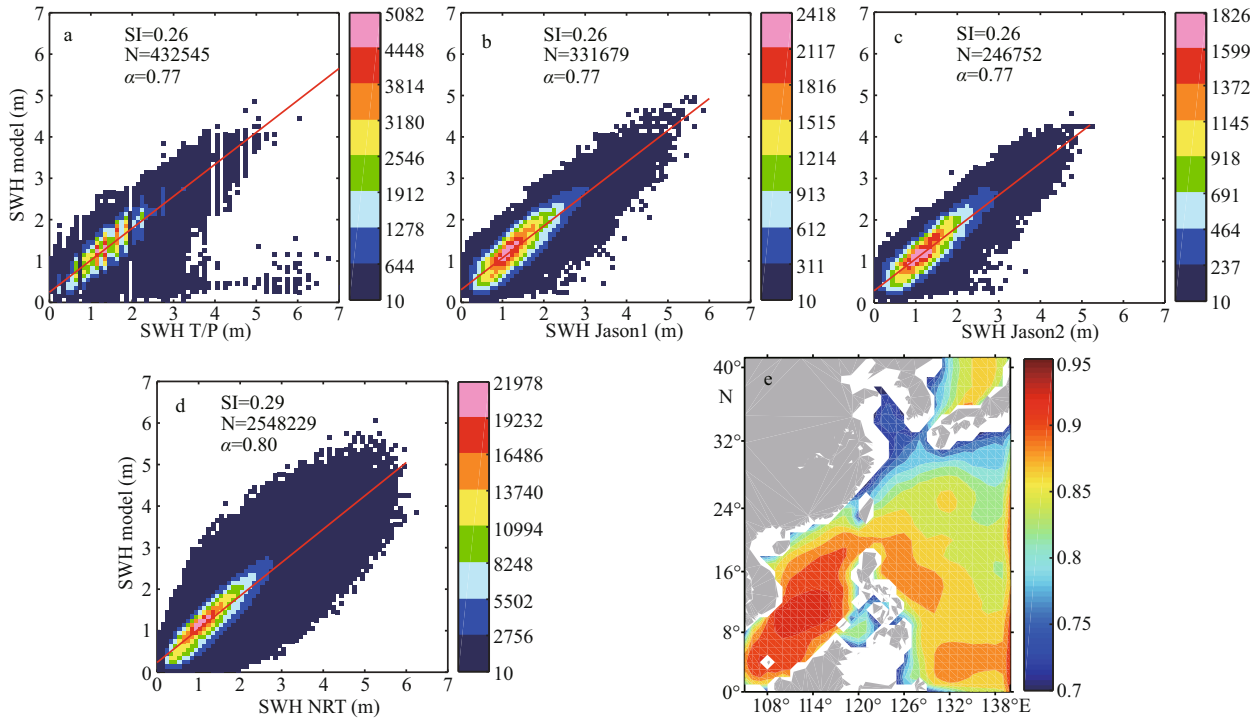

Fig.4 Scatter diagrams of the SWH (unit: m) hindcasted by the wave model and those observed by (a) TOPEX/Poseidon, (b) Jason-1, and (c) Jason-2, respectively; scatter diagram of the wave model hindcasted SWH (unit: m) and NRT-SWH (unit: m) (d); simultaneous correlation map between the daily time series of the model hindcasted SWH and NRT-SWH (e)

In a–d, *N* and *α* denote the number of selected grids and the slope of the least squares line, respectively. The color legend depicts the number of data within a 0.1×0.1 m grid box during the period of interest. Note that only correlations >0.70 above the 95% confidence level are presented in (e).

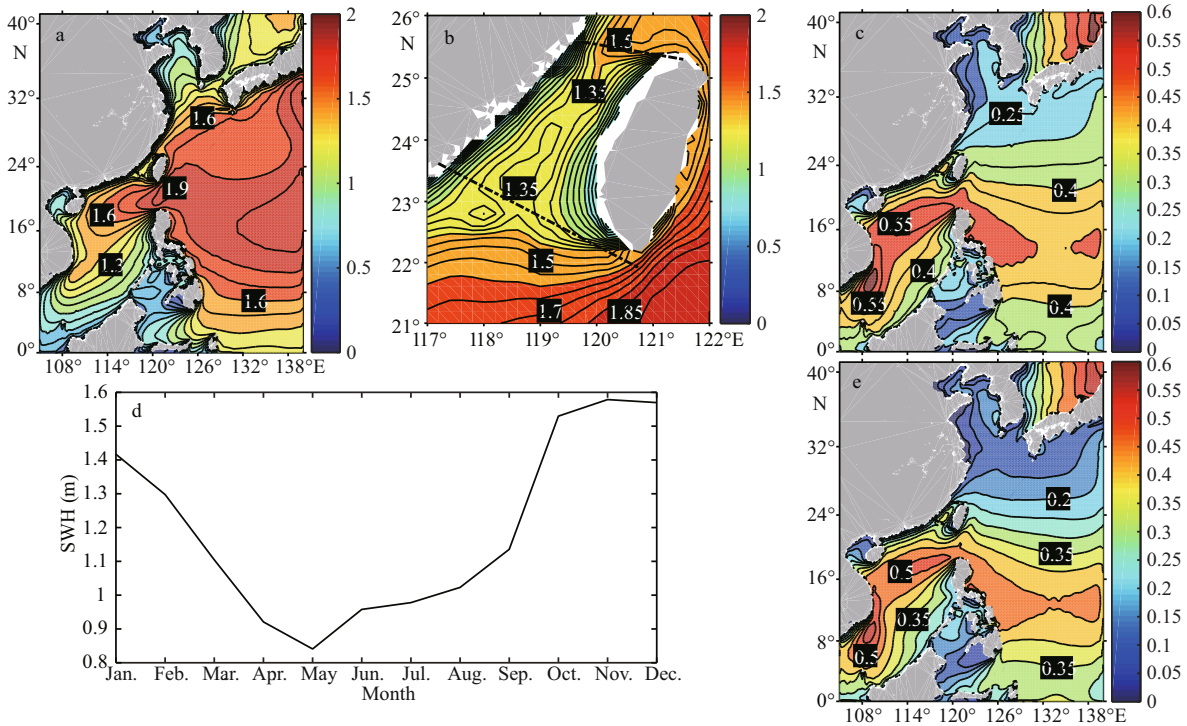

Fig.5 Climatological mean SWH (unit: m) over the China seas and adjacent waters (a), same as Fig.5a but over the TS (b), SD (unit: m) of the monthly SWH (c), climatological monthly SWH (unit: m) averaged over the entire TS (d), and SD of the climatological monthly SWH over the computation domain (e)

In (a) the contour interval is 0.1 m, whereas it is 0.05 m in (b), (c), and (e).

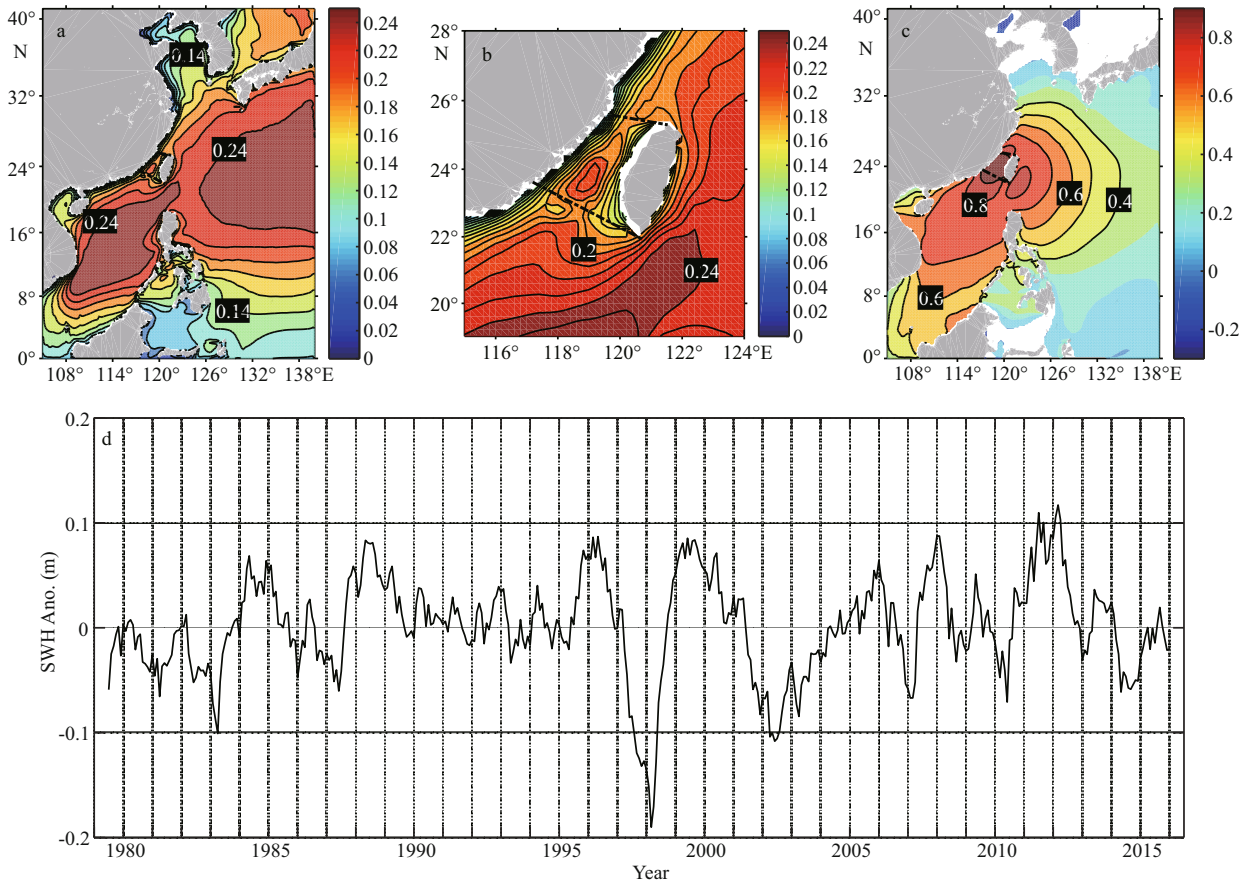

Fig.6 The SD of the interannual SWHA (unit: m) (a), same as Fig.6a but over the TS (b), simultaneous correlation coefficient between the interannual SWHA at each grid point and that averaged over the entire TS (only correlation coefficients above the 95% confidence level are presented) (c), and time series of the interannual SWHA (unit: m) averaged over the entire TS (d)

Contour intervals in (a), (b), and (c) are 0.02 m, 0.01 m, and 0.1, respectively.

Luzon Strait to east of the Vietnam coast in the SCS. The area-average SD of the SWH in the TS is about 0.32 m, while the maximum value, which occurs in the middle of the strait, is about 0.4 m.

The climatological monthly SWH averaged over the entire TS region is shown in Fig.5d. It can be seen that SWH in the TS has considerable seasonal variation, reaching a maximum of 1.58 m in November and a minimum of 0.84 m in May. This is consistent with historical observations (Guo et al., 2010). The SD of the climatological monthly SWH (Fig.5e) in the western North Pacific Ocean shows a similar spatial distribution to that of the monthly SWH (Fig.5c). In the TS, the SD of the climatological monthly SWH is also similar to that of the monthly SWH (Fig.5c). The area-averaged SD of the climatological monthly SWH over the entire TS is about 0.27 m, i.e., nearly equal to that of the monthly SWH. Therefore, the wave climate in the TS is dominated by the seasonal variation.

4.2 Interannual variability

The SD of the interannual SWH anomaly (SWHA) over the entire computation domain is shown in Fig.6. Overall, it is much smaller than that of the annual cycle (Fig.5e) and it has a different spatial distribution. There are two regions with high SD values of the interannual SWHA, which are located in the western North Pacific Ocean and along a northeast-southwest band in the middle of the SCS (Fig.6a). The SD of the interannual SWHA in the TS is relatively small and it is not spatially uniform (Fig.6b). It shows a regional maximum at around 23.8°N, 119.2°E, which is about 0.21 m smaller than in both the western North Pacific Ocean and the SCS. However, it is generally smaller than that of the annual cycle (Fig.5e). The area-averaged SD in the TS is only about 0.17 m, i.e., much smaller than that of the climatological monthly SWH.

The time series of the interannual SWHA averaged in the TS is presented in Fig.6d. It is considerably

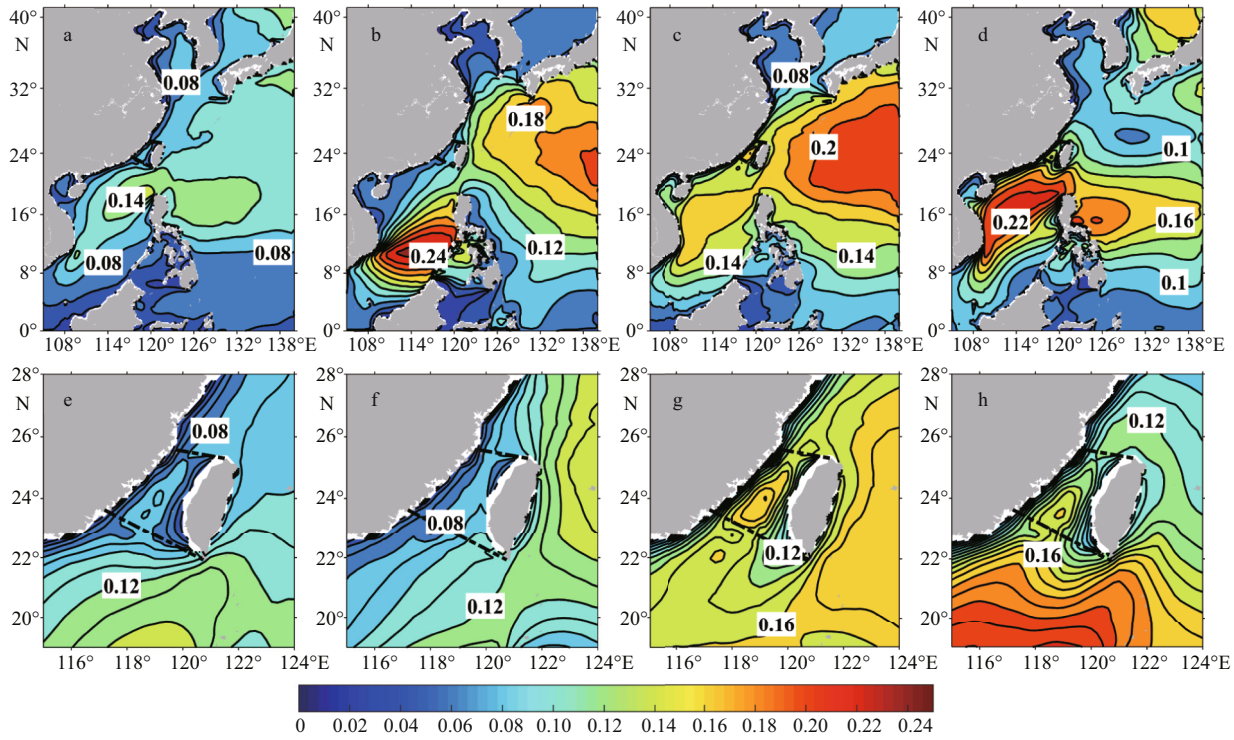

Fig.7 Maps of the SD of the seasonal mean SWHA (unit: m) in (a) spring, (b) summer, (c) autumn, and (d) winter in the western North Pacific Ocean and the adjacent China seas

(e)–(h) same as (a)–(d), respectively, but over the TS. Note, contour intervals in (a)–(d) and (e)–(h) are 0.02 m and 0.01 m, respectively.

negative during the years around 1983, 1986, 1991, 1997, 2009, and 2014 but positive during the years around 1984, 1988, 1998, 2007, and 2011. Given that El Niño or La Niña events occurred in these years, it could be expected that the interannual variability of SWH in the TS would be related strongly with ENSO events (as discussed in Section 4.4). The simultaneous linear correlation coefficients between the interannual SWHAs at all grid points around the TS and that averaged over the entire TS are shown in Fig.6c. Overall, the correlation coefficient is generally >0.9 in the TS and it then decreases away from the strait. The high correlation in the TS indicates that the entire TS shares nearly the same temporal variations in SWH on the interannual time scale. Therefore, the interannual SWHA averaged in the TS could be used to represent the interannual wave climate variability in the TS.

Maps of the SD of the seasonal mean SWHA in the four seasons are presented in Fig.7. In the current study, the seasons refer to those of the Northern Hemisphere, i.e., summer refers to June–August and winter refers to December–February. It can be seen from Fig.7 that the SDs of the seasonal mean SWHA in the TS are larger in autumn and winter than in the other two seasons. The area-averaged SDs of the seasonal mean SWHA in the TS in autumn and winter are 0.14 and 0.12 m, respectively, while those in summer and spring are 0.08 and 0.07 m, respectively. It means that the interannual SWH variability in the TS is much stronger in autumn and winter than in summer and spring. In spring, autumn, and winter, the spatial distributions of the SDs of the seasonal mean SWHA in the TS are similar to each other, with the highest values appearing in the middle of the strait. Outside the strait, the SD of the seasonal mean SWHA is generally high in the western North Pacific Ocean and the SCS. The SD maximum in the SCS always occurs around the Luzon Strait in all three seasons. However, in summer, the SD in the TS shows no regional maximum in the middle area. The SD maximum in the SCS occurs in the southern part, which is also markedly different from the other seasons. Therefore, the interannual SWH variability in summer might be markedly different from the other three seasons from the perspective of dynamics.

4.3 Dynamics

The temporal variation and spatial distribution of surface gravity waves are related closely to those of sea surface wind forcing (Xu et al., 2017). Hence, it is important to examine the relationship of the

Fig.8 Interannual anomalies of SWH (unit: m; black solid line) and sea surface wind speed (unit: m/s; black dashed line) averaged over the entire TS (a)

(b)–(e) same as (a) but for seasonal mean anomalies in spring, summer, autumn, and winter, respectively.

interannual SWH variability in the TS to sea surface wind forcing both inside and outside the TS. The interannual anomalies of SWH and sea surface wind speed (WS) averaged over the entire TS are compared in Fig.8a. Overall, they agree reasonably well, with the simultaneous linear correlation coefficient being about 0.76 above the 95% confidence level. However, it should be noted that they exhibit very different temporal phases during some periods, e.g., August–September 1990, July–August 1992, July–September 1998, and August 2004.

The seasonal mean anomalies of SWH and sea surface WS averaged over the TS in the four seasons are shown in Fig.8b–e. Interestingly, the correlation between SWH and sea surface WS in summer is markedly different from the other three seasons. In summer, the linear correlation coefficient is only about -0.17, implying no significant linear correlation between them. In the other three seasons, however, the linear correlation coefficients are all >0.75 above the 95% confidence level. The highest correlation occurs in winter (R=0.93). The different correlations suggest strongly that the dynamics responsible for the interannual SWH variability in summer should be markedly different from those in the other three seasons.

Previous studies have indicated that the TS is dominated by strong northeasterly monsoon winds from October to March in the following year, whereas the region is affected by weak southwesterly monsoon winds during the rest of the year (Chen et al., 2006; Guo et al., 2010). The above correlation analyses indicate that the interannual SWH variability in autumn, winter, and spring is mainly forced by the

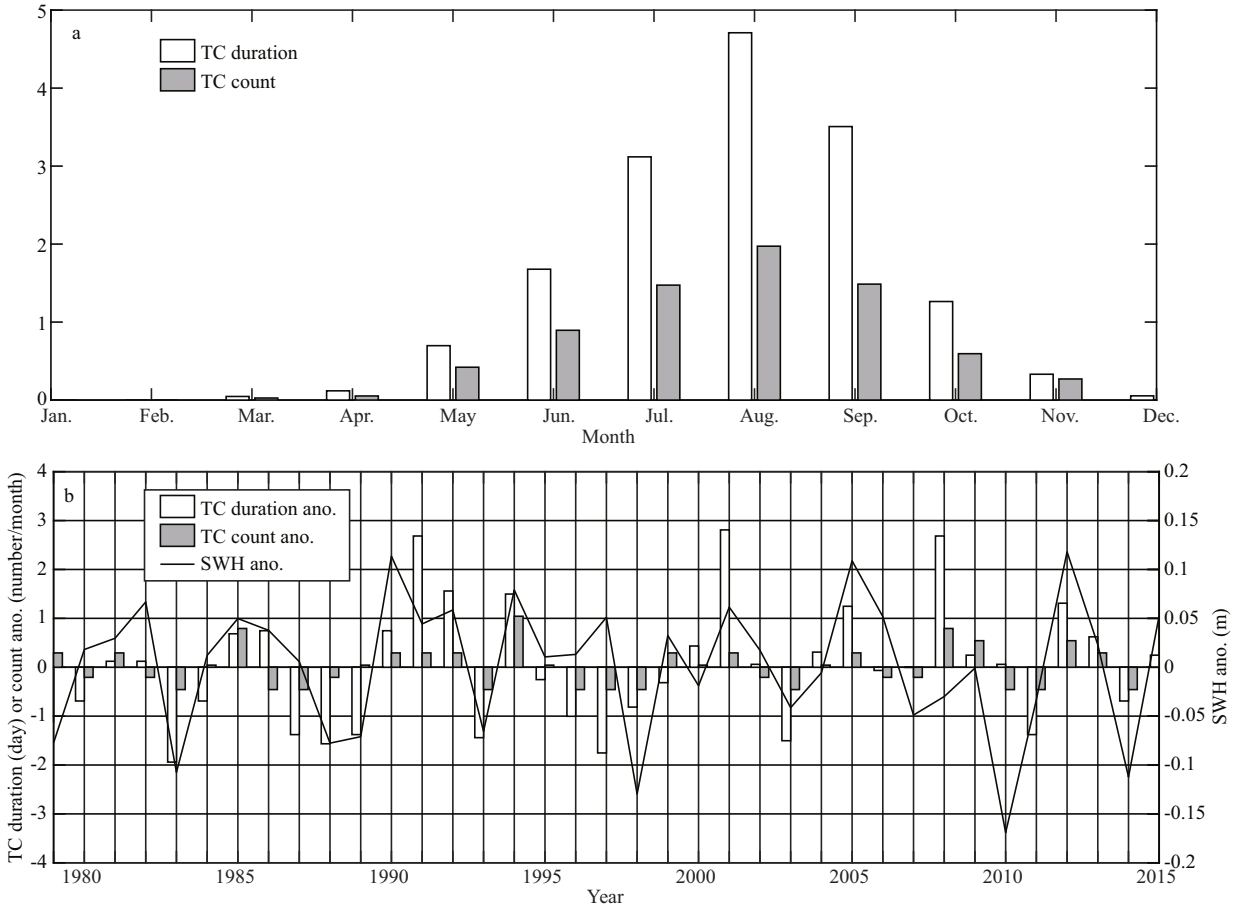

Fig.9 Climatological monthly frequency (unit: number in one month) and duration (unit: d) of TCs within the affected region (a), and summer mean anomalies of the frequency (unit: number in one month) and duration (unit: d) of TCs within the affected region and the SWH averaged in the TS (unit: m) (b)

northeasterly monsoon winds, while that in summer has no significant correlation with the southwesterly monsoon winds. The exact dynamics are discussed in the following.

4.3.1 Summer

In previous studies, many researchers have claimed that the TS and its adjacent areas are affected considerably by strong TC activities during summer, in addition to southwesterly monsoon winds (Ji et al., 2010). Given the poor correlation between the interannual SWH variability in the TS and the southwesterly monsoon winds, it is useful to examine whether TC activities make a significant contribution. For this analysis, we adopted the TC best-track dataset derived from the Regional Specialized Meteorological Center of the Japan Meteorological Agency (Needham et al., 2015).

Statistically, the maximum radii of regions with wind speeds of 30 kt (~15 m/s) when TCs pass are approximately 200–500 km (Fang et al., 1987; Hu et al., 2010), which is equivalent to 2°–5° in latitude or longitude. Therefore, we defined an affected region (19°–28°N, 115°–124°E) around the TS center of 23.5°N, 119.5°E. Thus, when a TC center was located within the affected region, the TC was considered to affect the wave field in the TS substantially. The climatological monthly frequency and duration (in days) of TCs that influence the TS are shown in Fig.9a (Sasaki et al., 2005; Bromirski et al., 2013). Here, the frequency was defined as the number of TCs in one month within the affected region. The duration was calculated as the number of days within one month when the TS was influenced by TCs. It can be seen that TCs occur mostly during June–September, and that the maxima of frequency and duration both occur in August. These findings are consistent with previous studies (Chan, 2005). Thus, in the following, summer refers to the months of June–September.

The time series of the summer mean anomalies of the frequency and duration of TCs influencing the TS are presented in Fig.9b, together with the SWHA

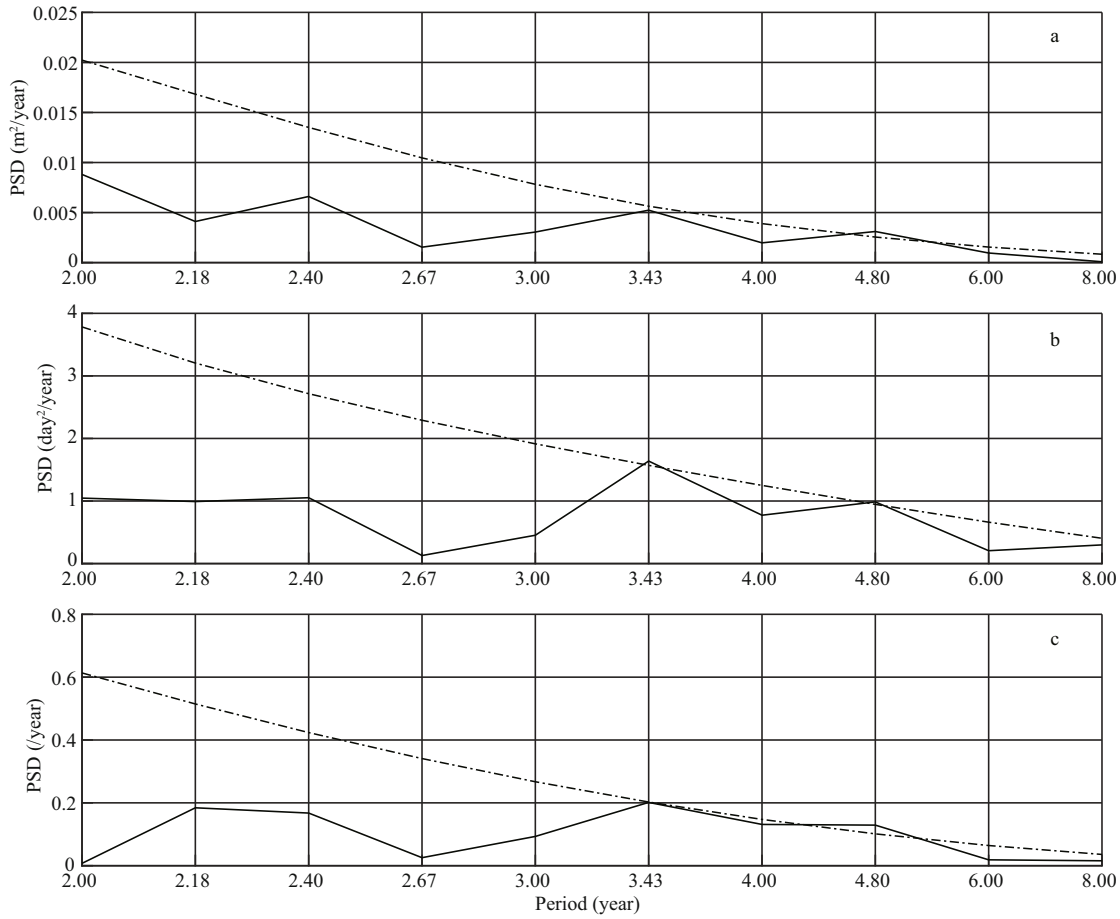

Fig.10 Power spectra of the summer mean anomalies of the SWH averaged in the TS (unit: m²/year) (a), the duration (unit: d²/year) (b), and frequency of the TCs (unit: /year) influencing the TS (c)

In each panel, the solid line denotes the power spectral density, while the dashed line represents the 95% confidence level for red noise.

averaged over the TS. It is interesting that the summer mean anomalies of both the frequency and duration of TCs show significant correlations with that of the SWH in the TS. Their simultaneous linear correlations are 0.52 and 0.55, respectively, both above the 95% confidence level. We also calculated the power spectra of the three variables (Bain, 1976) to explore their dominant varying periods (Fig.10). Interestingly, all three variables share a dominant varying period of about 4.8 years, which is significant at the 95% confidence level. This further suggests that the interannual SWH variability in summer in the TS is affected strongly by TC activities.

It should be noted that TCs are synoptic and that they have short durations within the affected region around the TS. This prompts the question of why the summer mean anomaly of SWH is correlated more significantly with TC activities than with the southwesterly monsoon wind. To investigate this, we calculated the mean wave energy in the TS in summer during days with and without TCs located in the affected region. We should note that the total wave energy in the summer season is proportional to the square of the summer mean SWH.

The time series of the summer mean wave energy (E) is plotted against that with TCs (E_T) and without TCs (E_M) in Fig.11a. These series were calculated as follows. The total wave energy, wave energy with TCs, and that without TCs in summer were first calculated based on the 6-hourly outputs (as described in Section 2.3). Then, the results were divided by the total number of time points in this season. As can be seen from the figure, E_T is much lower than E_M throughout the years of interest. However, the fluctuation of the former is much stronger than the latter. The SD of E_T is about 38.9 J/m², i.e., 49.2% higher than that of E_M, which is about 26.1 J/m². Meanwhile, E_T shows greater correlation with E (R=0.85) than does E_M (R=0.63). This implies strongly that E_T dominates the interannual variability of E in summer and hence, the interannual variability of the summer mean SWH. Figure 1b further compares the

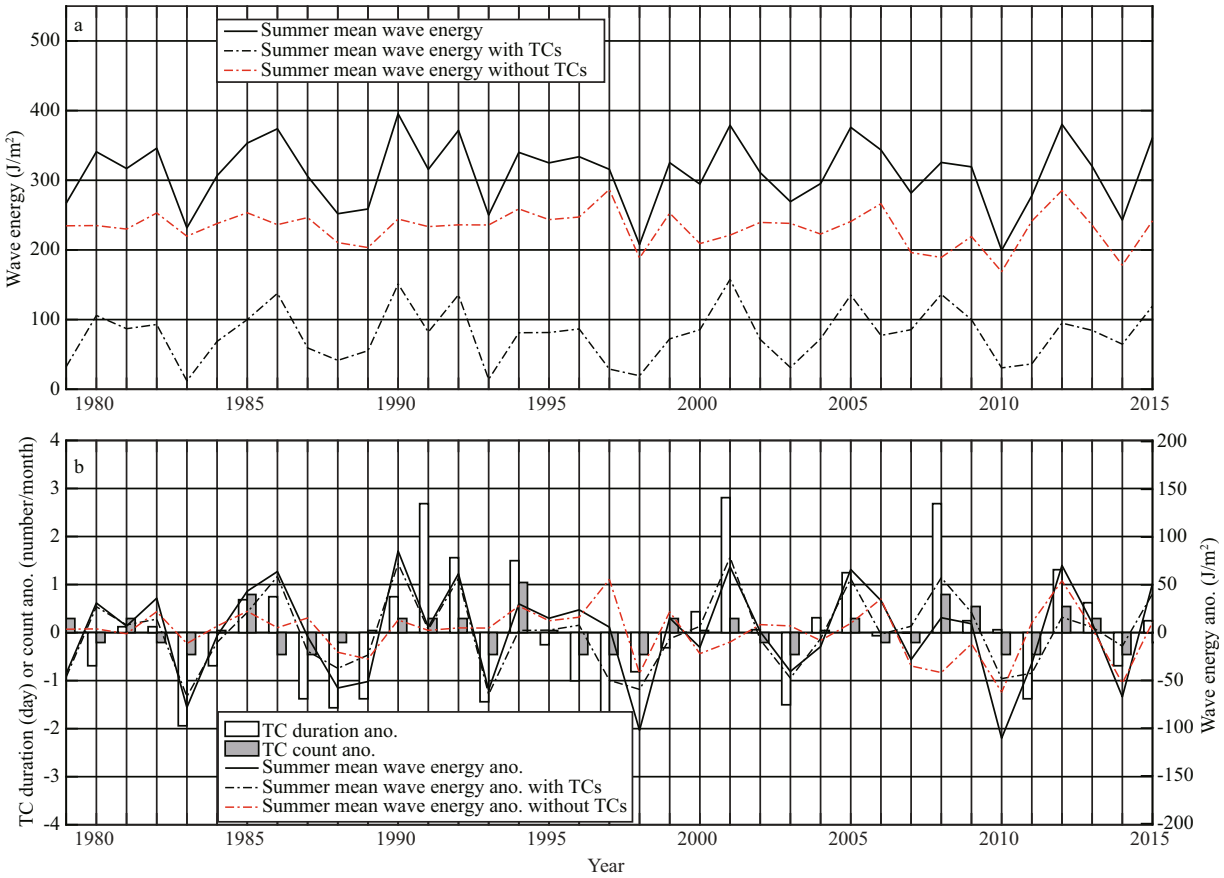

Fig.11 Time series of E (unit: J/m^2), E_T (unit: J/m^2), and E_M (unit: J/m^2) (a), and anomalies of E (unit: J/m^2), E_T (unit: J/m^2), E_M (unit: J/m^2) (b), and the frequency (unit: number in one month) and duration (unit: d) of TCs influencing the TS in the summer season

anomalies of the summer mean wave energy and those of TC properties. The dominance of E_T in the variations of E can be clearly seen. Their anomalies show reasonable agreement with each other in terms of both temporal phase and magnitude. Furthermore, anomalies of both the frequency and the duration of the TCs that influence the TS show significant correlations with the anomaly of E (R=0.60 and R=0.50, respectively). Therefore, we can conclude that TC activities dominate the interannual variability of SWH in the TS in summer, while the southwesterly monsoon winds make a secondary contribution.

4.3.2 Winter

In winter, the TS is dominated by northeasterly surface gravity waves under the forcing of northeasterly monsoon winds (figure not shown). In the following, given the months of the prevailing northeasterly monsoon winds, winter denotes the months of October–March. As shown in Fig.8, in the TS, the SWHAs are correlated significantly with the local sea surface WS anomalies in autumn, winter, and spring when the northeasterly monsoon winds prevail. Meanwhile, Fig.7 shows that the SD maxima of the seasonal mean SWHA occur in the middle area of the TS during these seasons. Therefore, it would appear that the interannual SWH variabilities in these seasons are controlled mainly by local sea surface wind forcing in the TS.

To investigate this point, we conducted another model simulation with a smaller computation domain. In the following discussion, the model simulation using the large computation domain, as shown in Fig.1a, is denoted CTR, while that using the small computation domain is denoted EXR. The model configurations of EXR were mostly the same as CTR, except with regard to the computational domain and the boundary conditions. As shown in Fig.1b, the computational domain of EXR covers the region 21°–26°N, 117°–122°E. Free boundary conditions were applied to all ocean boundaries of the EXR domain.

The climatological mean SWH (H_{EXR}) output by EXR is presented in Fig.12a. It can be seen that the spatial distribution of H_{EXR} outside the TS is notably

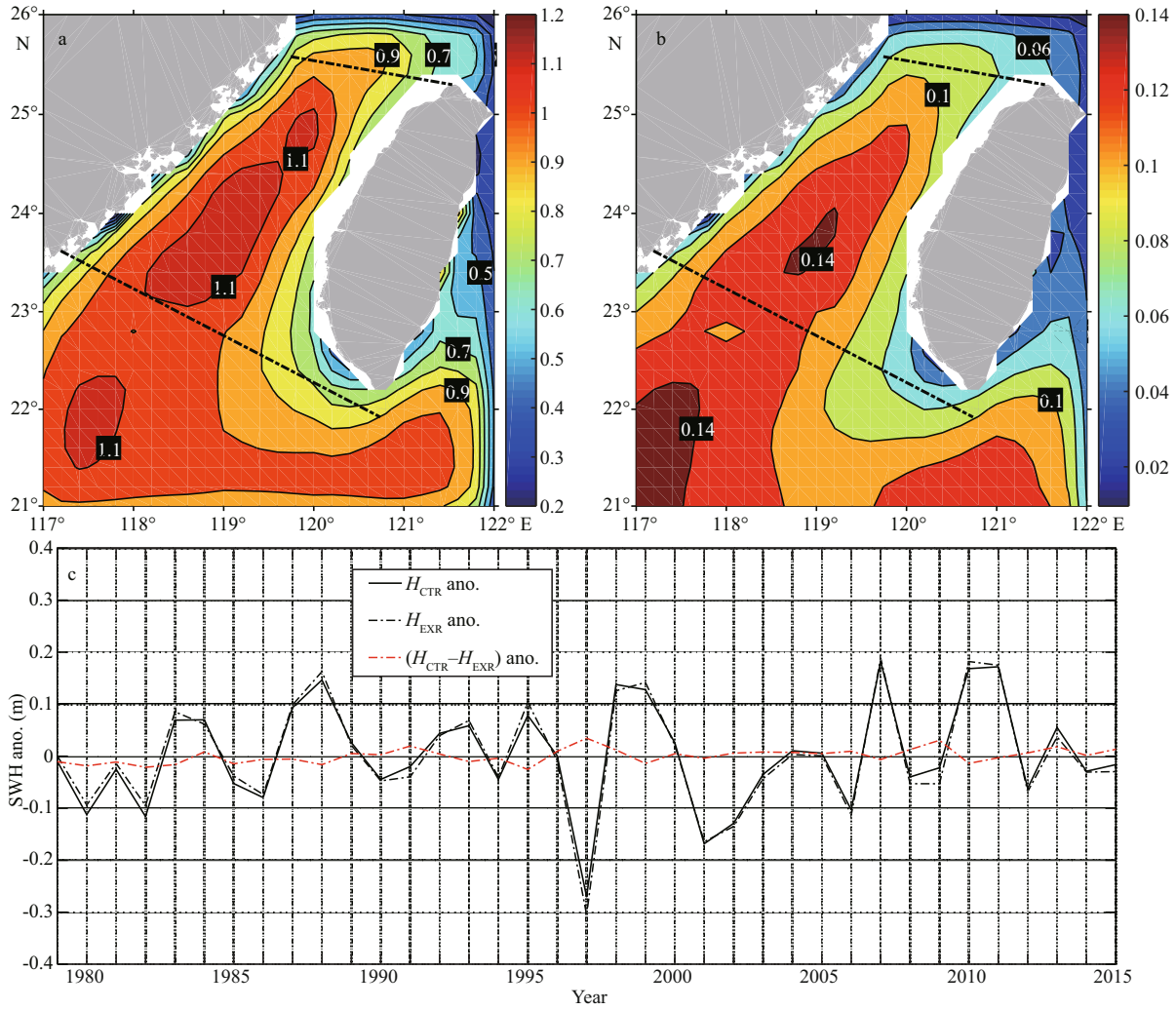

Fig.12 Climatological mean SWH output by EXR (H_{EXR}; unit: m) (a). The contour interval is 0.1 m. SD of the mean anomalies of H_{EXR} (unit: m) in the northeasterly monsoon seasons (b). The contour interval is 0.02 m. Time series of the mean anomalies of the area-averaged H_{CTR} (unit: m; black solid line), H_{EXR} (unit: m; black dashed line), and (H_{CTR}–H_{EXR}) (unit: m; red dashed line) in the TS in the northeasterly monsoon seasons (c)

different from that of the climatological mean SWH (E_{CTR}) output by CTR (Fig.5b) because of the small computation domain and free boundary conditions of EXR. However, the spatial distributions of the climatological means H_{EXR} and H_{CTR} inside the TS are similar, i.e., H_{EXR} in the TS is also largest in the middle area and it then decreases shoreward. Overall, H_{EXR} is slightly smaller than H_{CTR}. The largest value of H_{EXR} in the TS is 1.18 m, which is 15.7% lower than the largest value of H_{CTR} (1.40 m). Moreover, the area-averaged H_{EXR} over the TS is about 0.95 m, which is 20.2% lower than the area-averaged H_{CTR} (1.19 m). Furthermore, during the northeasterly monsoon seasons, the SD of the mean anomalies of H_{EXR} (Fig.12b) is also similar to that derived from the CTR simulation (Fig.7e, g, and h) in terms of both spatial distribution and magnitude, i.e., it shows high values in the middle area of the strait. The area-averaged SD of H_{EXR} over the TS is about 0.11 m, reasonably similar to that of H_{CTR}.

Figure 12c further compares the time series of the mean anomalies of the area-averaged H_{CTR} and H_{EXR} in the TS during the northeasterly monsoon seasons. As expected, they agree reasonably well with each other in terms of both temporal variation and magnitude. Their simultaneous linear correlation is about 0.99 above the 99% confidence level, and their SDs are 0.11 and 0.10 m, respectively. Their difference is shown as the red dashed line, which has an approximately zero average with the SD being 0.01 m. Therefore, it is suggested strongly that the wave climate in the TS during the northeasterly monsoon seasons is controlled by local sea surface wind forcing.

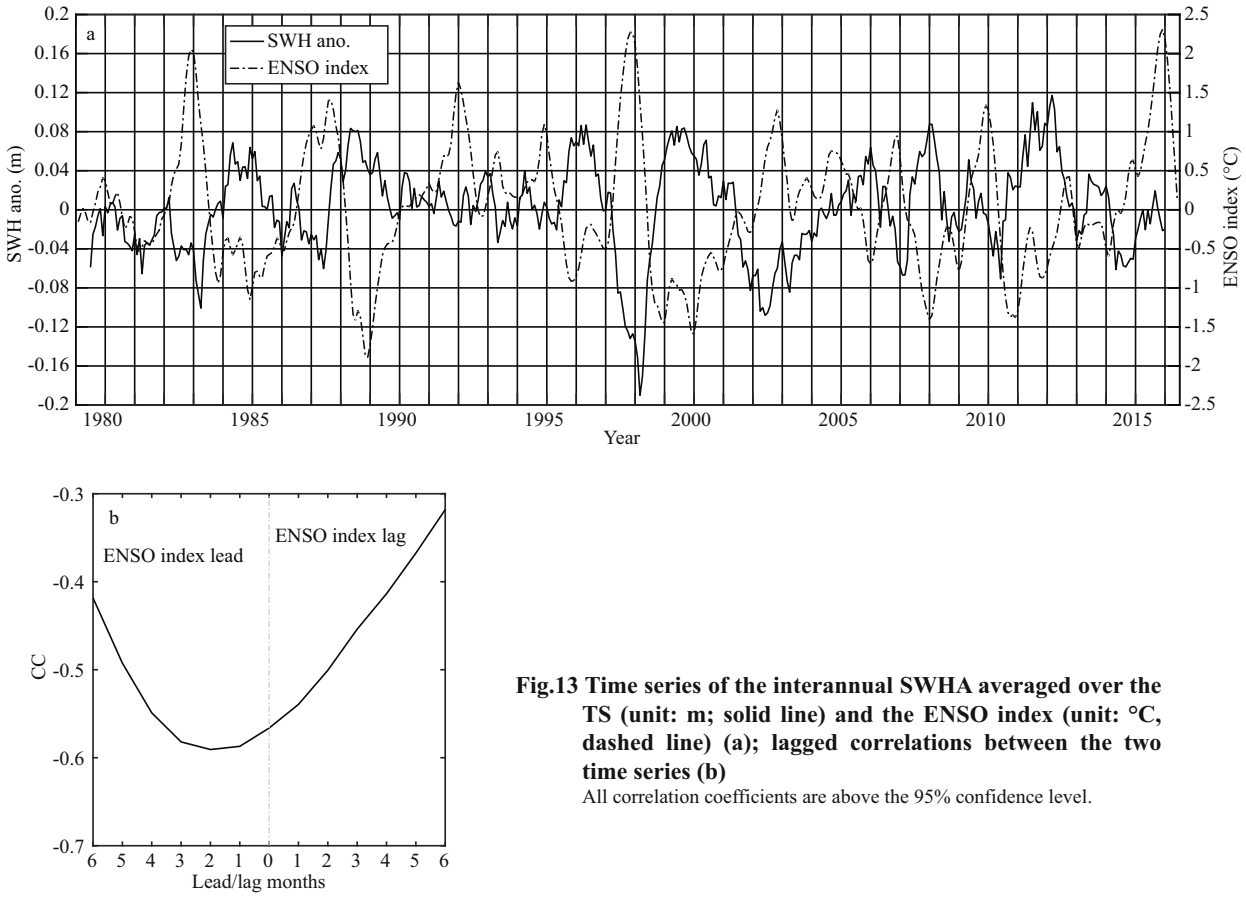

Fig.13 Time series of the interannual SWHA averaged over the TS (unit: m; solid line) and the ENSO index (unit: °C, dashed line) (a); lagged correlations between the two time series (b)
All correlation coefficients are above the 95% confidence level.

4.4 Relationship to ENSO

Previous studies have shown that the interannual variability of the SWH around the Taiwan Island is modulated by the ENSO cycle (Chien et al., 2014). Therefore, it is meaningful to examine further the potential relationship between interannual wave climate variability in the TS and the ENSO phenomenon.

The time series of the ENSO index and the interannual SWHA averaged over the TS, compared in Fig.13a, generally show variations with opposite phases. During strong El Niño years (e.g., 1982/1983, 1991/1992, and 1997/1998), SWH in the TS shows significantly negative anomalies, while during La Niña years (e.g., 1984/1985, 1988/1989 and 1998/1999), positive anomalies of SWH are evident. We calculated the lagged correlations between the two time series. As shown in Fig.13b, the monthly SWH anomaly is correlated highly negatively with the ENSO index (R=-0.60) above the 95% confidence level when the latter leads the former by about two months. Meanwhile, their simultaneous correlation is about -0.58 above the 95% confidence level. This is similar to the situation at the Longdong buoy station, which is located to the northeast of Taiwan Island. Based on buoy observations, Chien et al. (2014) indicated that the annual mean of the anomalies of SWH at the Longdong station is correlated highly positively (R=0.48) above the 95% confidence level with the annual mean Southern Oscillation index.

As discussed in Section 4.3, the dynamics responsible for the interannual wave climate variability in the TS in summer are markedly different from winter. Therefore, it is helpful to examine the relationships in these two seasons.

4.4.1 Summer

The lagged correlation between the summer mean SWHA and the ENSO index is shown in Fig.14. It can be seen that the summer mean SWHA is correlated moderately positively with the ENSO index (R=0.44) above the 90% confidence level with no significant time lags. This is notably different from that between the interannual SWHA and the ENSO index shown in Fig.13b.

As discussed in Section 4.3.1, the interannual wave climate variability in the TS during summer is controlled predominantly by TC activities. Therefore, the significantly positive correlation between the summer mean SWHA and the ENSO index implies

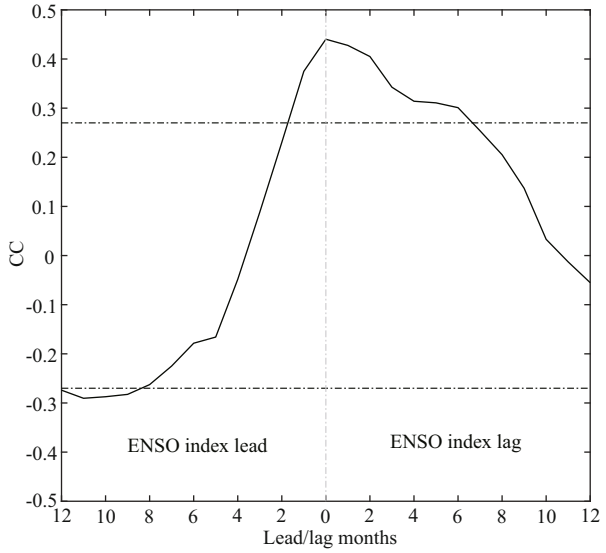

Fig.14 Lagged correlation (solid line) between the ENSO index and the summer mean SWH anomaly averaged over the TS

Dashed lines indicate correlation coefficients at the 90% confidence level.

that TC activity in the western North Pacific Ocean and the adjacent seas is correlated highly positively with the ENSO index. Indeed, previous studies have revealed a pronounced relationship between ENSO events and TC activities in the western North Pacific Ocean and the adjacent seas (Chan, 1985, 2000; Dong, 1988; Lander, 1994; Chen et al., 1998). During El Niño summers, more TCs with longer life spans tend to form in the eastern part of the northwestern Pacific Ocean before following a curving path toward the ECS and Japan (Chan, 1985, 2000; Dong, 1988; Lander, 1994; Elsner and Liu, 2003; Chu, 2014), resulting in significantly intensified TC activities over the TS. During La Niña summers, however, TCs tend to form in areas further west before tracking westward or west-northwestward across the Philippines and the SCS (Elsner and Liu, 2003), resulting in weakened TC activities over the TS.

4.4.2 Winter

The lagged correlation between the winter mean SWHA and the ENSO index is shown in Fig.15a. Different from the situation in summer, the winter mean SWHA shows significantly negative correlation with the ENSO index (R=-0.49) above the 90% confidence level when the latter leads the former by about one month. This is similar to that between the total time series of the interannual SWHA and the ENSO index shown in Fig.13b.

As discussed in Section 4.3.2, the interannual wave climate variability in the TS in winter is controlled predominantly by the northeasterly monsoon winds. Therefore, the above negative correlation suggests strongly that interannual monsoon wind variability over the TS should be correlated negatively with the ENSO index. Simultaneous regression maps of the winter mean anomalies of sea surface wind vectors and wind speeds against the normalized winter mean ENSO index are displayed in Fig.15b. The most prominent feature in the regression map is the existence of significant anticyclonic wind anomalies over the far western Pacific Ocean and the SCS. The southwesterly wind anomalies over the TS reduce the northeasterly winter monsoon there, inducing negative sea surface wind speed anomalies. To elucidate this, we calculated the composite winter mean anomalies of sea surface wind vectors and surface wind speeds during both El Niño years (Fig.15c) and La Niña years (Fig.15d). The results agree reasonably well with the above regression maps (Fig.15b). During El Niño winters, there are significant anticyclonic wind anomalies over the western Pacific Ocean and the SCS. Over the TS, the southwesterly wind anomalies lead to significantly negative anomalies in sea surface wind speed; however, during La Niña years, the situation is reversed.

The weaker (stronger) than normal winter monsoon along the East Asian coast during El Niño (La Niña) years has already been noted in previous studies (Tomita and Yasunari, 1996; Zhang et al., 1996; Ji et al., 1997). From the perspective of dynamics, it is forced by the lower-tropospheric anomalous anticyclone (cyclone) that is present over the western Pacific Ocean and the SCS during El Niño (La Niña) years (Wang et al., 2000; Wang and Zhang, 2002; He and Wang, 2013).

5 CONCLUSION

Based on the output of a high-resolution numerical wave model, this study investigated the characteristics and underlying dynamics of the interannual wave climate variability in the TS. The results demonstrated that the interannual variability of SWH in the TS is weaker than the seasonal variability. Generally, the SD of the interannual SWHA is largest in the middle of the strait and it then decreases shoreward. It shows similar spatial distributions throughout the year, except in summer, when there is no regional maximum in the middle of the strait. Such results might imply that the interannual SWH variability in summer is markedly different from that in the other seasons from the perspective of dynamics.

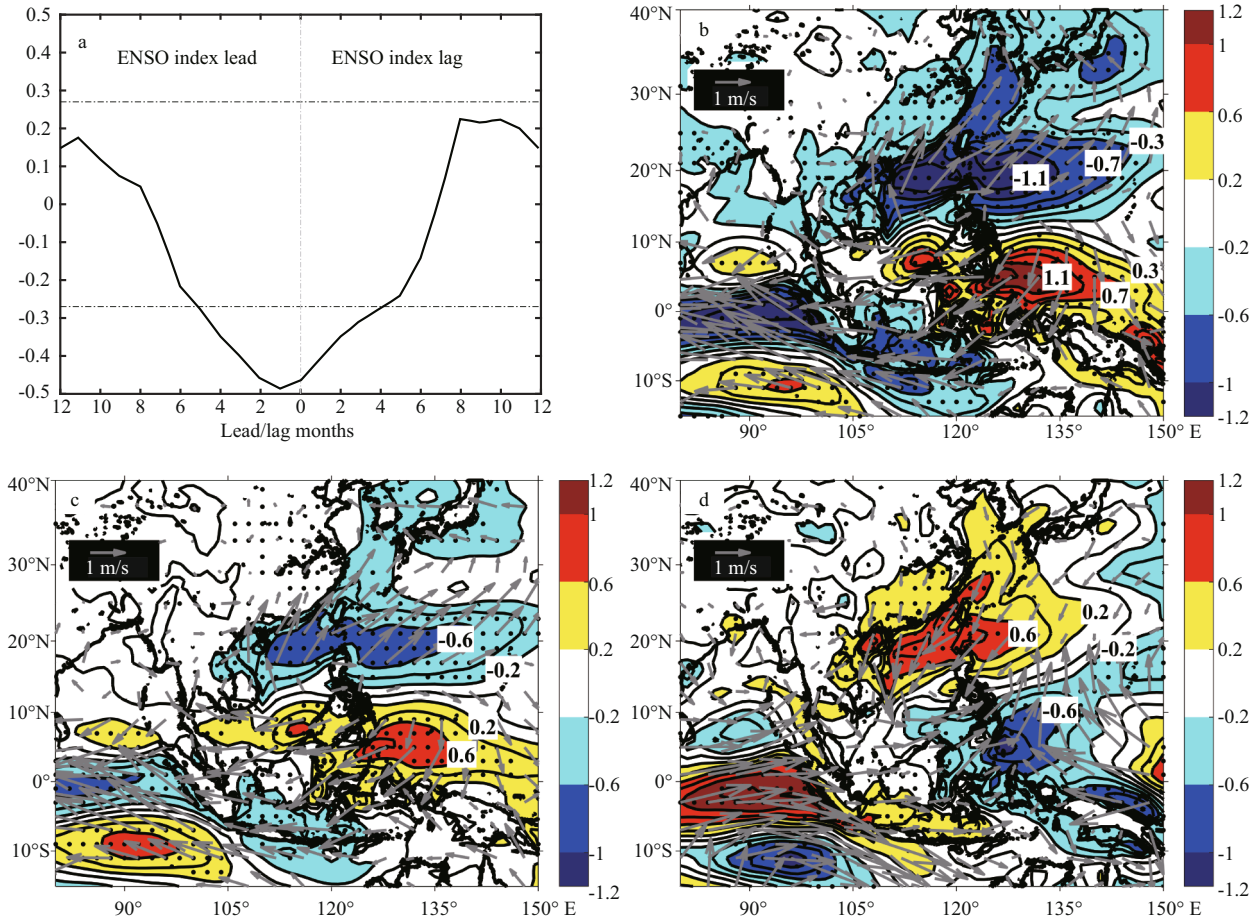

Fig.15 Same as Fig.14 but between the ENSO index and winter mean SWHA averaged over the TS (a). Simultaneous regression maps of the winter mean anomalies of sea surface wind vectors (gray arrow; unit: m/s) and wind speeds (color; unit: m/s) over the western Pacific Ocean and the adjacent seas against the normalized winter mean Nino3.4 index (b). Composite winter mean anomalies of sea surface wind vectors (gray arrow; unit: m/s) and wind speeds (color; unit: m/s) during El Niño years (c). Same as (c) but during La Niña years (d)

In (b)–(d), the contour interval is 0.2 m/s and the black dots denote the results above the 95% confidence level based on a two-sided Student's *t*-test.

As sea surface gravity waves are all generated by sea surface wind forcing, the relationship between the interannual variations of the monthly mean SWH and sea surface wind speed over the TS was examined. Unexpectedly, the interannual SWH anomaly showed very low correlation with that of the monthly mean sea surface wind speed in summer when southwesterly monsoon winds prevail. During the northeasterly monsoon seasons, however, the correlations were very significant. This further suggests that the underlying dynamics responsible for the interannual wave climate variability in the TS are different during the southwesterly monsoon season in comparison with the northeasterly monsoon seasons. Indeed, further analysis indicated that the interannual wave climate variability in the TS in summer is controlled predominantly by TC activities, while that in winter is forced by northeasterly monsoon winds.

We also explored the relationship of the interannual wave climate variability in the TS with the ENSO phenomenon, which is the most active large-scale climatic variability in the tropical Pacific Ocean. Overall, the interannual SWHA in the TS showed significant correlation with the ENSO index (R= -0.60) above the 95% confidence level when the former lagged the latter by about two months. This relationship is derived mainly from that during the northeasterly monsoon seasons. During the northeasterly monsoon seasons in El Niño (La Niña) years, there is a lower-tropospheric anomalous anticyclone (cyclone) over the western Pacific Ocean and the SCS (e.g., Wang et al., 2000; Wang and Zhang, 2002). This anomalous anticyclone (cyclone) largely weakens (strengthens) the northeasterly monsoon winds in the TS, resulting in negative (positive) SWHA there. During the summer season in

El Niño years, however, more TCs with longer life spans tend to form in eastern parts of the northwestern Pacific Ocean before following a curving path toward the ECS and Japan (Chan, 1985, 2000; Dong, 1988; Lander, 1994; Elsner and Liu, 2003; Chu, 2014). Intensified TC activities over the TS induce a significant positive SWHA. During La Niña summers, however, TCs tend to form in areas further west before following westward or west-northwestward tracks across the Philippines and the SCS (Elsner and Liu, 2003), resulting in weakened TC activities over the TS.

6 DATA AVAILABILITY STATEMENT

The details of the data that support the findings of this study are described in Section 2, including the providers and websites from which the data can be downloaded freely.

7 ACKNOWLEDGEMENT

The authors would like to thank Dr. LIU Cong of the Ocean University of China for providing helpful advice during this work, from guidance on its structure to editing of the paper.

References

Bain W C. 1976. The power spectrum of temperatures in central England. *Quarterly Journal of the Royal Meteorological Society*, **102**(432): 464-466.

Battjes J A, Janssen J P F M. 1978. Energy loss and set-up due to breaking of random waves. *In*: Proceedings of the 16th International Conference on Coastal Engineering Conference. American Society of Civil Engineers, Hamburg, Germany. p.569-587.

Booij N, Ris R C, Holthuijsen L. 1999. A third-generation wave model for coastal regions: 1. Model description and validation. *Journal of Geophysical Research*: *Oceans*, **104**(C4): 7 649-7 666.

Bromirski P D, Cayan D R, Helly J, Wittmann P. 2013. Wave power variability and trends across the North Pacific. *Journal of Geophysical Research*: *Oceans*, **118**(12): 6 329-6 348.

Chan J C L. 1985. Tropical cyclone activity in the northwest Pacific in relation to the El Niño/Southern Oscillation phenomenon. *Monthly Weather Review*, **113**(4): 599-606.

Chan J C L. 2000. Tropical cyclone activity over the western North Pacific associated with El Niño and La Niña events. *Journal of Climate*, **13**(16): 2 960-2 972.

Chan J C L. 2005. Interannual and interdecadal variations of tropical cyclone activity over the western North Pacific. *Meteorology and Atmospheric Physics*, **89**(1-4): 143-152.

Chang C K, Chien C C. 2001. The studies of the typhoon wave characteristic at the eastern coast of Taiwan. *In*: Asian and Pacific Coastal Engineering. Dalian University of Technology Press, Dalian, China. p.70-77.

Chen G, Chapron B, Ezraty R, Vandemark D. 2002. A global view of swell and wind sea climate in the ocean by satellite altimeter and scatterometer. *Journal of Atmospheric and Oceanic Technology*, **19**(11): 1 849-1 859.

Chen H X, Hua F, Yuan Y L. 2006. Seasonal characteristics and temporal variations of ocean wave in the Chinese offshore waters and adjacent sea areas. *Advances in Marine Science*, **24**(4): 407-415. (in Chinese with English abstract)

Chen T C, Weng S P, Yamazaki N, Kiehne S. 1998. Interannual variation in the tropical cyclone formation over the western North Pacific. *Monthly Weather Review*, **126**(4): 1 080-1 090.

Chen X, Sha W Y, Min J Z. 2002. The simulation of typhoon waves around Taiwan Island. *Marine Forecasts*, **19**(4): 1-10. (in Chinese with English abstract)

Chien H, Cheng H Y, Chiou M D. 2014. Wave climate variability of Taiwan waters. *Journal of Oceanography*, **70**(2): 133-152.

Chu P S. 2014. ENSO and tropical cyclone activity. https://www.researchgate.net/publication/255578707. Accessed on 2014-10-22.

Dee D P, Uppala S M, Simmons A J, Berrisford P, Poli P, Kobayashi S, Andrae U, Balmaseda M A, Balsamo G, Bauer P, Bechtold P, Beljaars A C M, van de Berg L, Bidlot J, Bormann N, Delsol C, Dragani R, Fuentes M, Geer A J, Haimberger L, Healy S B, Hersbach H, Hólm E V, Isaksen L, Kållberg P, Köhler M, Matricardi M, McNally A P, Monge-Sanz B M, Morcrette J J, Park B K, Peubey C, de Rosnay P, Tavolato C, Thépaut J N, Vitart F. 2011. The ERA-interim reanalysis: configuration and performance of the data assimilation system. *Quarterly Journal of the Royal Meteorological Society*, **137**(656): 553-597.

Dong K. 1988. El Niño and tropical cyclone frequency in the Australian region and the northwest Pacific. *Australian Meteorological Magazine*, **36**: 219-225.

Eldeberky Y. 1996. Nonlinear Transformation of Wave Spectra in the Nearshore Zone. Delft University of Technology, Delft, The Netherlands. 203p.

Elsner J B, Liu K B. 2003. Examining the ENSO-typhoon hypothesis. *Climate Research*, **25**(1): 43-54.

Fang W L, Xu Q M, Zhang J L, Tan C B. 1987. Distribution of the wind speed in typhoons over the East China Sea. *Marine Forecasts*, **4**(3): 1-14. (in Chinese with English abstract)

Feng S Z, Li F Q, Li S J. 2010. An Introduction to Marine Science. Higher Education Press, Beijing, China. p.435-437. (in Chinese)

Guo T T, Gao W Y, Gao Y, Gong F. 2010. An analysis of the climate characteristics for Taiwan Strait. *Marine Forecasts*, **27**(1): 53-58. (in Chinese with English abstract)

Hasselmann K, Barnett T P, Bouws E, Carlson H, Cartwright D E, Enke K, Ewing J A, Gienapp H, Hasselmann D E,

Kruseman P, Meerburg A, Müller P, Olbers D J, Richter K, Sell W, Walden H. 1973. Measurements of wind-wave growth and swell decay during the Joint North Sea Wave Project (JONSWAP). Deutches Hydrographisches Institut, Hamburg, *Germany*. p.1-95.

Hasselmann S, Hasselmann K, Allender J H, Barnett T P. 1985. Computations and parameterizations of the nonlinear energy transfer in a gravity-wave specturm. Part II: parameterizations of the nonlinear energy transfer for application in wave models. *Journal of Physical Oceanography*, **15**(11): 1 378-1 391.

He S P, Wang H J. 2013. Oscillating relationship between the East Asian winter monsoon and ENSO. *Journal of Climate*, **26**(24): 9 819-9 838.

Hu B H, Yang X Q, Tan Y K, Wang Y Q, Fan Y. 2010. A new method for calculating the wind speed distribution of a moving tropical cyclone. *Advances in Atmospheric Sciences*, **27**(1): 69-79.

Huang B Y, Banzon V F, Freeman E, Lawrimore J, Liu W, Peterson T C, Smith T M, Thorne P W, Woodruff S D, Zhang H M. 2014. Extended reconstructed sea surface temperature version 4 (ERSST.v4): Part I: upgrades and intercomparisons. *Journal of Climate*, **28**(3): 911-930.

Hwang C H, Yao C C, Lee W C. 2010. Evaluation of wave energy changes in Taiwan. *In*: Proceedings of the International Conference on Energy and Sustainable Development: Issues and Strategies. IEEE, Chiang Mai, Thailand. p.1-6.

Jan S, Tseng Y H, Dietrich D E. 2010. Sources of water in the Taiwan Strait. *Journal of Oceanography*, **66**(2): 211-221.

Jan S, Wang J, Chern C S, Chao S Y. 2002. Seasonal variation of the circulation in the Taiwan Strait. *Journal of Marine Systems*, **35**(3-4): 249-268.

Ji H D, Pan W R, Zhang G R. 2010. Numerical simulation of tyhpoon waves in Taiwan Strait and Xiamen Bay. *Marine Forecasts*, **27**(1): 44-48. (in Chinese with English abstract)

Ji L R, Sun S Q, Arpe K, Bengtsson L. 1997. Model study on the interannual variability of Asian winter monsoon and its influence. *Advances in Atmospheric Sciences*, **14**(1): 1-22.

Jiang H Y, Chen G. 2013. A global view on the swell and wind sea climate by the *Jason-1* mission: a revisit. *Journal of Atmospheric and Oceanic Technology*, **30**(8): 1 833-1 841.

Jiang T S, Ren J L, Shen C Q. 2014. Simulation of significant wave height in the shallow shelf area by SWAN model and its improvement. *Marine Forecasts*, **31**(4): 9-17. (in Chinese with English abstract)

Komen G J, Hasselmann S, Hasselmann K. 1984. On the existence of a fully developed wind-sea spectrum. *Journal of Physical Oceanography*, **14**(8): 1 271-1 285.

Lander M A. 1994. An exploratory analysis of the relationship between tropical storm formation in the western North Pacific and ENSO. *Monthly Weather Review*, **122**(4): 636-651.

Lin Y H, Fang M C. 2012. The assessment of ocean wave energy along the coasts of Taiwan. *China Ocean Engineering*, **26**(3): 413-430.

Needham H F, Keim B D, Sathiaraj D. 2015. A review of tropical cyclone-generated storm surges: global data sources, observations, and impacts. *Reviews of Geophysics*, **53**(2): 545-591.

Sasaki W, Iwasaki S I, Matsuura T, Lizuka S. 2005. Recent increase in summertime extreme wave heights in the western North Pacific. *Geophysical Research Letters*, **32**(15): L15607.

Tomita T, Yasunari T. 1996. Role of the northeast winter monsoon on the biennial oscillation of the ENSO/monsoon system. *Journal of the Meteorological Society of Japan*, **74**(4): 399-413.

Wang B, Wu R G, Fu X H. 2000. Pacific-East Asian teleconnection: how does ENSO affect East Asian climate? *Journal of Climate*, **13**(9): 1 517-1 536.

Wang B, Zhang Q. 2002. Pacific-East Asian teleconnection. Part II: how the Philippine sea anomalous anticyclone is established during El Niño development. *Journal of Climate*, **15**(22): 3 252-3 265.

Wang C Z, Deser C, Yu J Y, DiNezio P, Clement A. 2016. El Niño and southern oscillation (ENSO): a review. *In*: Glynn P W, Manzello D P, Enochs I C eds. Coral Reefs of the Eastern Tropical Pacific. Springer, Dordrecht, The Netherlands. p.85-106.

Xu Y, Bi F, Song J B, He H L. 2017. The temporal and spatial variations in the Pacific wind and wave fields for the period 2002-2011. *Acta Oceanologica Sinica*, **36**(3): 26-36.

Yamaguchi M, Hatada Y, Ohfuku M, Li M J, Nonaka H. 2002. 51-year wave hindcast and analysis of wave height climate trend on the northwestern Pacific Ocean. *Journal of Japan Society for Natural Disaster Science*, **20**(4): 435-448.

Zhang G Y, Zhang X D, Yu M G. 2002. Characteristics and distribution pattern of wind and wave in sea area of Taiwan. *Marine Science Bulletin*, **21**(1): 23-30. (in Chinese with English abstract)

Zhang R H, Sumi A, Kimoto M. 1996. Impact of El Niño on the East Asian monsoon: a diagnostic study of the '86/87 and '91/92 events. *Journal of the Meteorological Society of Japan*, **74**(1): 49-62.

Zheng C W, Chen X, Li C Y. 2016. Observation of wave climate in surrounding waters of Taiwan Island. *Journal of PLA University of Science and Technology*: *Natural Science Edition*, **17**(5): 473-479. (in Chinese with English abstract)

Zheng C W, Pan J, Tan Y K, Gao Z S, Rui Z F, Chen C H. 2015. The seasonal variations in the significant wave height and sea surface wind speed of the China's seas. *Acta Oceanologica Sinica*, **34**(9): 58-64.

Zhou H, Roarty H, Wen B Y. 2015. Wave height measurement in the Taiwan Strait with a portable high frequency surface wave radar. *Acta Oceanologica Sinica*, **34**(1): 73-78.

Table A1 Descriptions of the abbreviations used in the paper

Abbreviation	Description	Abbreviation	Description
EAM	East Asia Monsoon	SI	Scatter indexes
ECS	East China Sea	SWAN	Simulating WAves Nearshore
ENSO	El Niño-Southern Oscillation	SWH	Significant wave height
ERA-I	European Centre for Medium-Range Weather Forecasts Interim reanalysis	SWHA	SWH anomaly
NRT-SWH	Near-real time merged SWH	TC	Tropical cyclone
SCS	South China Sea	TS	Taiwan Strait
SD	Standard deviation	WS	Wind speed